An investigation on the free vibration behaviors of additively manufactured PA6 layered plates: influences of stacking sequence, infill ratio, and boundary conditions

Sinan Maraş
Ondokuz Mayıs University, Faculty of Engineering, Department of Mechanical Engineering, 55270, Samsun, Türkiye
sinan.maras@omu.edu.tr, https://orcid.org/0000-0002-2651-374X

Çağın Bolat
Samsun University, Faculty of Engineering and Natural Sciences, Department of Mechanical Engineering, 55420, Samsun, Türkiye
cagin.bolat@samsun.edu.tr, https://orcid.org/0000-0002-4356-4696

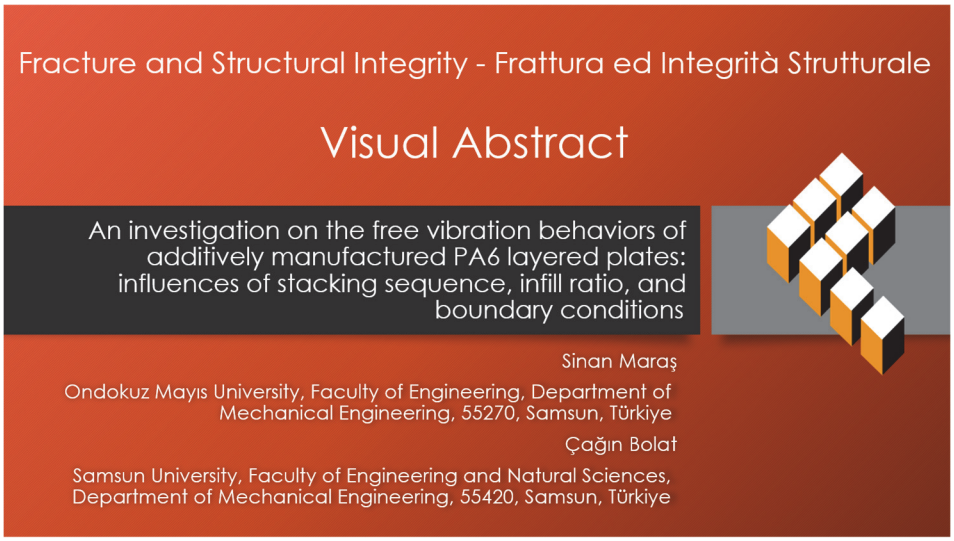

Citation: Maraş, S., Bolat, Ç., An investigation on the free vibration behaviors of additively manufactured PA6 layered plates:
influences of stacking sequence, infill ratio, and boundary condition, Fracture and Structural Integrity, 73 (2025) 200-218.

Received: 04.05.2025
Accepted: 01.06.2025
Published: 04.06.2025
Issue: 07.2025

KEYWORDS. Polyamides, Fused filament fabrication, Stacking sequence, Infill ratio, Natural frequency, Finite element methods.

INTRODUCTION

In today's technology-oriented and competitive globe, rising customer requirements inevitably urge scientists, researchers, and manufacturing engineers to develop novel, low-cost, environmentally friendly, and swift production strategies. Even though conventional manufacturing techniques such as drilling, turning, welding, casting, roll-forming, forging, and extrusion are commonly used and operated in many industrial areas, other innovative advanced methods have also become popular lately to attain a longer, safer, and more precise working response for a specific machine element. Right at this point, layer-by-layer accumulation systems, which form the ultimate object by additive manufacturing (AM), can be proposed as one of the most attractive techniques. On account of its fast-prototyping ability [1], rapid fabrication capability [2], versatility for creating intricate shapes [3], and clean manufacturing concept [4], almost all of the AM ways are tried and examined in the scientific archives by different project groups to show their forcefulness when they are checked up with

other traditional techniques. In this context, it is not difficult to estimate that technical studies on this promising research area will escalate in the next years, and interestingly, there are still lots of critical areas holding to be explored.
Among the whole AM versions, the fused filament fabrication (FFF) method can be seen as the most favored method due to its implementation comfort, low-expenditure system needs, swift manufacturing potential, and efficient interaction with automation-based installations [5]. If the main workflow of the FFF technology is detailed, typically, it involves certain principal stages: technical drawing of component design through a suitable computer-aided design (CAD) program, transferring the CAD information to the proper slicing software for nozzle movement, extrusion of the fused polymer filament via an automatically moving printhead, removal of the target object from baseline, and post-processing operations [6]. When it comes to the suitable polymers, thermoplastic grades are utilized frequently in the FFF or FFF-related methodologies. Commonly, acrylonitrile butadiene styrene (ABS), polylactic acid (PLA), polyethylene terephthalate glycol (PETG), polyether ether ketone (PEEK), and polyamide (PA) are featured filaments both in scientific efforts and industrial trials [7]. This inclination emerges from certain critical responses of these materials like low melting temperature (below 200°C), perfect fluidity, and satisfactory viscosity. What's more, these thermoplastics carry a strong potential for numerous implementations from pharmacy and dentistry to aviation and automotive [8].
In recent periods, many inspiring and precious scholarly projects have been performed to scrutinize the physical, structural, and mechanical performance of FFF-based thermoplastic samples. Parallel to this, dissimilar investigation teams exerted to reveal the tensile, flexural, hardness, and fatigue features of FFF-printed products while the others spent efforts to address dimensional accuracy efficiency [9]. On the other side, tribological characteristics of printed objects made by FFF technology were also analyzed by some investigators [10]. In addition, as the FFF allows the fabrication of fiber-reinforced polymers (short or continuous carbon and glass fibers) [11], scientific articles related to this topic are notably high too. Although it is a highly crucial property for structural and elastic properties of design components, the number of technical efforts on the subject of natural frequency and vibration responses can be qualified as limited and must be investigated to block the unwanted damping problems, specifically in 3D-printed polymers. Interestingly, this trend has started to shift lately, and some research groups reported noteworthy results for FFF-printed samples. For instance, Parpala, Popescu [12] stated that infill rate was an important factor in measuring the natural frequency values of FFF-printed ABS samples, and the increasing number of contours in the printing stage resulted in lower natural frequency results. Öteyaka, Çakir [13] noted that 3D-printed PLA samples displayed the best vibration damping outcomes in the cross type infill pattern in comparison with the other patterns like grid and tri-hexagon. Chaitanya, Reddy [14] emphasized the mixed influence of the layer thickness and building direction on the damping and vibration results of ABS specimens. Bolat, Çebi [15] fabricated recycled PETG tests samples by FFF method to dig out their natural frequency levels and put forth that there was a negative interaction between the infill rate and the measured natural frequency results. Monkova, Monka [16] prepared ABS samples with lattice structures using an FFF system and underlined that the natural frequencies found via experimental and operational modal analysis were, in most cases, lower than those achieved with the finite element method. Azmi, Ismail [17] concentrated on a similar topic and ABS lattice material to indicate the positive relationship between the stiffness of the test material and calculated natural frequency values. In another effort, Kannan, Manapaya [18] probed the effect of fiber reinforcements on the vibration responses of PLA samples and announced that the carbon-added PLA showed a 25% rise in elastic modulus and a 17% increase in natural frequencies compared to plain PLA.
In this paper, different from the previous scientific efforts, for the first time in the technical literature, the vibration behavior of 3D-printed layered PA6 plate samples was analyzed in terms of unlike stacking sequences, dissimilar infill ratios, and different loading conditions by making experimental pre-analyses and finite element approaches. Considering the real-time loading conditions of 3D-printed PA6 samples like gears, fan blades, and arm mechanisms, structural stability, vibration regime, and noise reduction are highly critical properties that can adjust the general efficiency of the design component, as well as long-life service performance and sufficient energy usage. Herein, as a unique initiative, the combined effect of the printing variables, boundary conditions, and composite design versatility was evaluated meticulously to comprehend the frequency nature of difficult-to-print material of PA6 by performing experimental mechanical work and detailed finite element methods.

MATERIALS AND METHODOLOGY

Printing material properties

PA6, also known as Nylon 6, is a well-known thermoplastic polymer belonging to the family of nylon-based plastics. Typically, it involves a recurring amide group in the chain structure. In point of structural properties, it possesses a semi-crystalline inner phase distribution, which enables its relatively high mechanical responses like moderate/high

tensile strength and good impact endurance. What's more, PA6 is one of the most preferred materials for composite matrix structures because of its perfect merging capacity with glass or carbon fibers to form strong composites. Recently, this potential has been used for 3D-printing applications by different research teams, too.
Printed PA6 filaments were procured by Microzey Limited Company (Istanbul, Turkey). From the technical knowledge of the supplier firm, certain featured physical and mechanical properties of the filaments are depicted in Tab. 1 given below.

Property	PA6
Colour	Black
Diameter (mm)	1.75
Density (m^3/kg)	1120
Bed Temperature (°C)	110
Printing Temperature (°C)	270
Tensile Strength (MPa)	67
Elongation at Break (%)	15

Table 1: Specification of PA6 filaments

3D Printing Procedures

Before the layer-by-layer production stage, CAD models of the PA6 tensile specimens were drawn through SolidWorks 2020® software, looking at the related standard. As serial uniaxial tensile tests are conducted, ASTM D368 Type-4 standards were adopted. After the CAD design, the solid model data was sent to the Flashprint 5.0 slicing program to create target g-codes. Fig. 1 shows the technical dimensions of the produced samples.

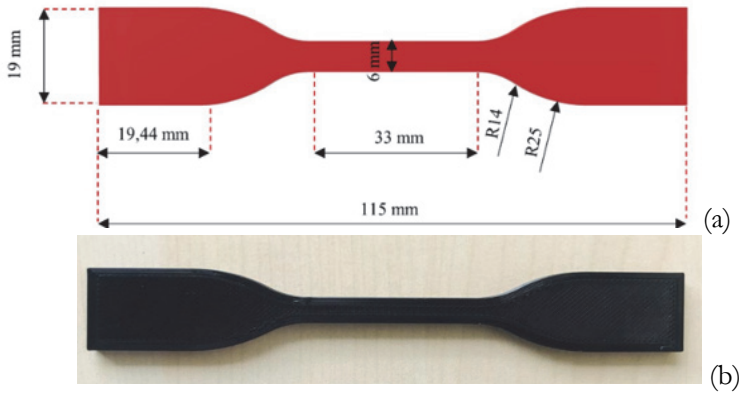

Figure 1: Dimensions of the test samples (a) and printed sample (b)

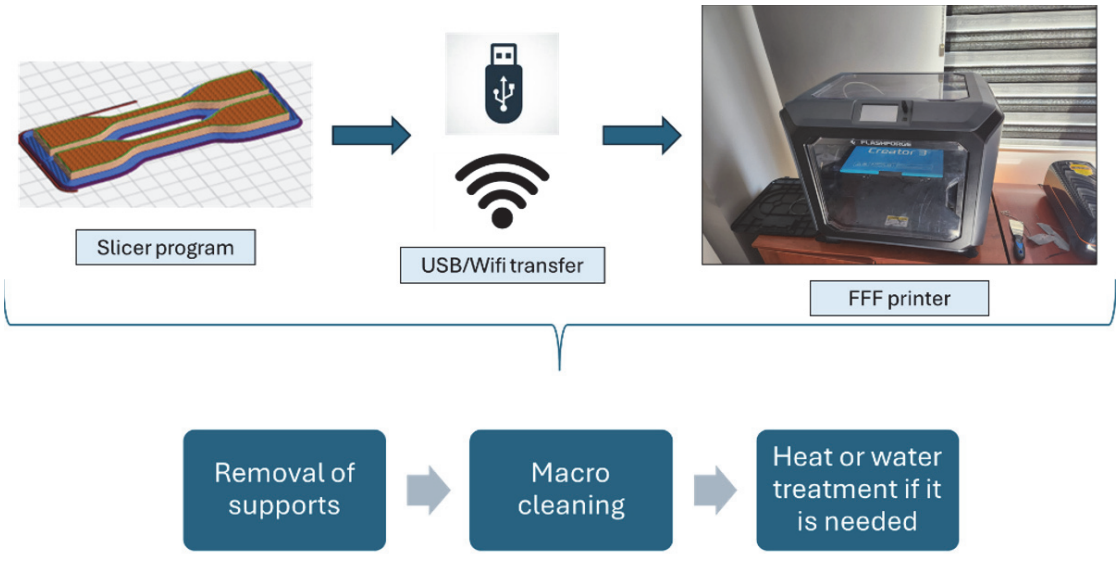

Figure 2: Process flow in the FFF stage.

Using the adjusted g-codes, PA6 samples were fabricated via the Flashforge Creator 3 3D printer (Zhejiang Flashforge 3D Technology Co. Ltd., China). The utilized printing machine possesses a flexible accumulation bed with a magnet (300x250x200 mm print size). Also, the highest plate temperature of 120 °C can be obtained via this printer (maximum nozzle temperature of 320 °C and the fastest print speed of 150 mm/s). Further, by way of its closed cabin ambient, the mean moisture level of the cabin was controlled, and unstable cooling gradients were hindered. Tab. 2 and Fig. 2 indicate all of the input variable details in the additive manufacturing step and production flowline, respectively.

Parameter	PA6
Infill (%)	40; 70; 100
Infill pattern	Hexagon
Build direction	Horizontal
Cabin type	Close
Raft (mm)	1
Fan speed (%)	100
Layer height (mm)	0.27
Shell count	3
Support	None

Table 2: Printing parameters utilized in the FFF.

Test and simulation studies

All tensile tests were conducted using the Besmak BMT-E300 uniaxial test machine and related special software. Firstly, the force and stroke values were collected from the software. After that, the engineering stress and engineering strain values were obtained by utilizing the initial dimensions of the test specimens. Depending on these data, stress/strain curves were created. During the tests, a 5 mm/min deformation rate was applied, and all of them were realized in the room conditions.

Vibration analysis of 3D printed plates with ANSYS

The dynamic behavior of 3D printed PA6 layered plates was investigated using the finite element method implemented in ANSYS software. The simulation employed the SHELL 281 element (Fig. 3a), which is an 8-node shell element, each node possessing six degrees of freedom—three translational and three rotational (in the x, y, and z directions). This element type is well-suited for the analysis of thin-walled structures. Mechanical properties obtained from tensile tests were assigned to the model, assuming the material to be linear, elastic, and isotropic. The mechanical anisotropy occurs in the FDM parts depending on the printing directions and loading direction as a result of the nature of layer-by-layer production. However, for thinner design parts, this effect decreases and some literature efforts ([12, 19, 20] that focuses on the similar research area reported that isotropic models also could be applied. For 3D-printed parts, elastic modulus is critical for natural frequency value and both isotropic and transversely isotropic models can be applied according to literature works [21]. For these reasons, an isotropic material model has been considered in this study. The finite element mesh was composed of 1225 elements and 3816 nodes. Fig. 3b and 3c present a representative ANSYS model of one of the layered plates. Modal analysis was carried out to determine the natural frequencies of the structure through numerical computation. Fig. 4 illustrates the geometry of the 3D printed PA6 sandwich plate along with the reference axes of the layers.

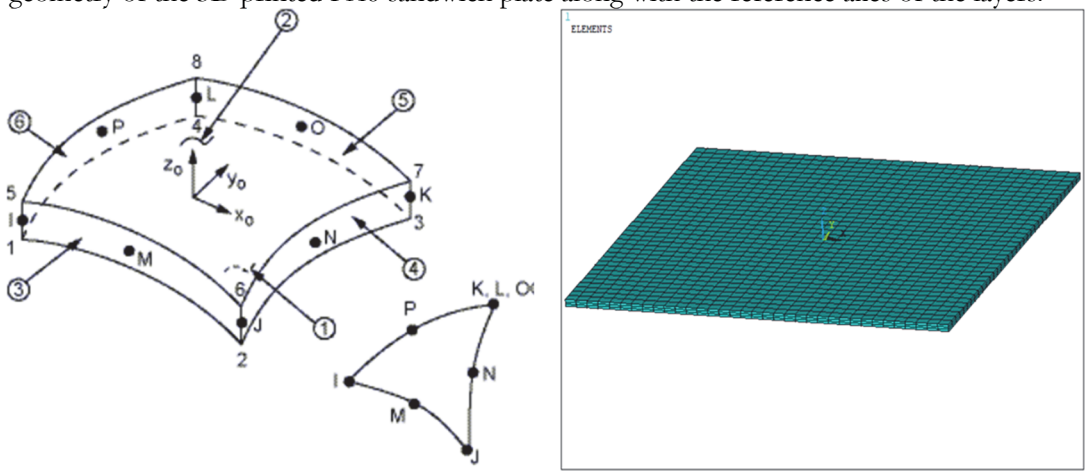

a) b)

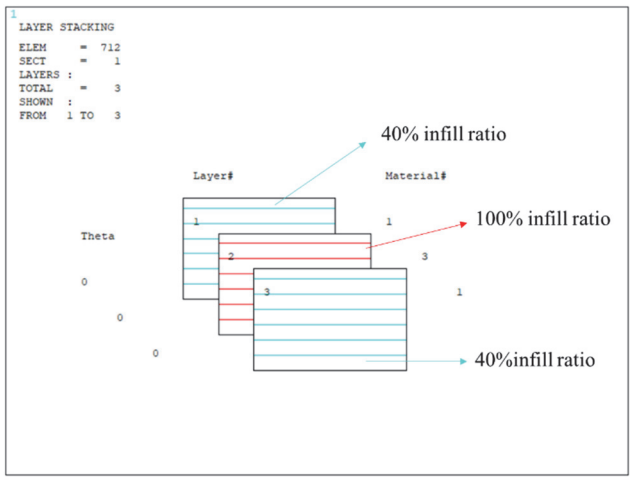

c)

Figure 3: ANSYS model of the 3d printed PA6 layered plate: a) SHELL 281 element, b) ANSYS model of the configuration with a 40%-100%-40% infill ratio and CCCC boundary conditions, c) Sequence of the layered element.

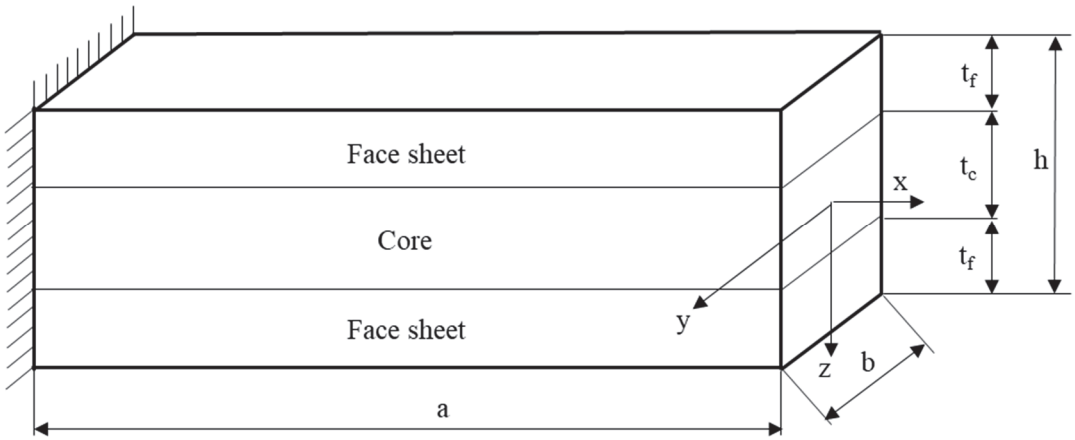

Figure 4: The geometry of the 3D printed PA6 sandwich plate with reference axes of the layers.

In this study, the effects of infill ratios (40%, 70%, and 100%), aspect ratios (a/b = 1, 1.5, 2, and 2.5), and boundary conditions (fully clamped — CCCC, and simply supported — SSSS, respectively) on the free vibration behavior of 3D printed PA6 three-layered plates with various configurations were numerically investigated. The mechanical properties of the additively manufactured PA6 material were determined through tensile tests, as presented in Figs. 5 and 6. In the study, the thicknesses of the layers in the examined plates were equal and set to 0.001 m. Furthermore, the plate length was kept constant at a = 0.2 m. As shown in Tab. 3, analyses were conducted for nine different layered 3D-printed PA6 plate configurations by considering three different infill ratios (40%, 70%, and 100%).

Configurations	Name
40%-40%-40%	A
40%-70%-40%	B
40%-100%-40%	C
70%-70%-70%	D
70%-40%-70%	E
70%-100%-70%	F
100%-100%-100%	G
100%-40%-100%	H
100%-70%-100%	I

Table 3: Various 3D-printed PA6 plate configurations with distinct layering sequences.

RESULTS AND DISCUSSION

Mechanical experiments and density evaluations

Fig. 5 shows the engineering stress/engineering strain curves of the produced PA6 samples according to altering infill ratios. The highest average ultimate tensile strength of 22.9 MPa was calculated for the samples built via 100 % infill ratio while the lowest average tensile strength of 19.3 MPa belonged to the sample printed with 40 % infill ratio. Similar trends were also recorded for the elastic modulus outcomes as seen in Fig. 6. At this point, 0.31, 0.35, and 0.43 GPa results were found for the samples having 40 %, 70 %, and 100 % filling rates respectively. From the results, it is true to emphasize that there is an affirmative relationship between the infill ratio and measured mechanical properties of 3D-printed samples. Parallel findings were also reported by other investigation teams [22]. Looking at the general deformation of the fabricated samples, these results can be explained by the rising load-carrying polymer ratio of the fully-filled samples depending on the damage modes. For the samples possessing high production gaps, relatively easy merging of printing voids are also responsible for the observed tensile strength trends.

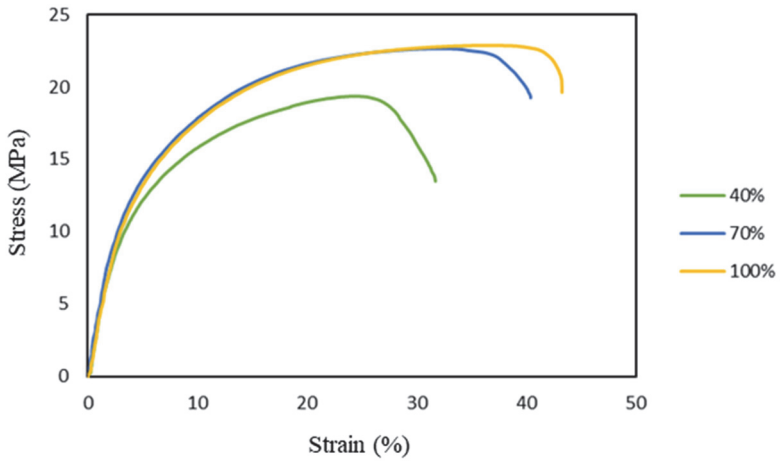

Figure 5: Engineering stress/strain curves of PA6 parts depending on infill ratios.

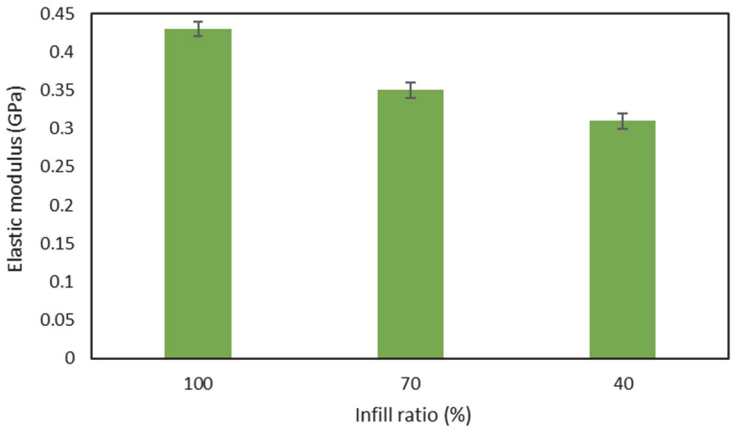

Figure 6: Elastic modulus results depending on infill ratios.

Fig. 7 demonstrates the average density values of the produced PA6 samples together with the shifting infill ratio values. Indeed, even if the whole samples are manufactured with 100 % filling rate, additional production gaps can form between the stacking layers and accumulation-based contact points as a result of the layer-by-layer building nature of FFF process. Therefore, it can be estimated that as the infill ratio parameter gets smaller the calculated average density results dwindle due to the synergetic effect of production gaps and printing pattern. Glancing at Fig. 7, it is seen that the highest density value of 1.02 g/cm^3 can be noticed for the sample formed with 100 % infill ratio while the lowest value of 0.83 g/cm^3 was

measured for the samples fabricated with 40 %. On the other side, for the moderate infill percentage value of 70 %, the average value of 0.94 g/cm³ was determined that was 11.7 % higher than the samples with 40 % infill ratio and 8.5 % lower than the fully-filled samples.

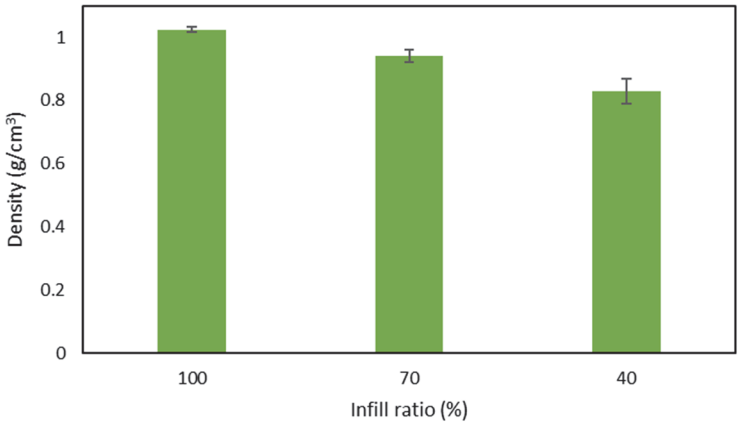

Figure 7: Density results of PA6 parts depending on infill ratios.

Validation study

Before performing the vibration analysis of PA6 Layered Plates Produced by Additive Manufacturing, the validation study of the model created in the Ansys finite element package program was carried out by comparing it with the studies in the literature. Firstly, free vibration analysis of the plate made of aluminum material with four simply supported edges was performed. The material properties are defined as follows:
E=70x109 Gpa, ϱ=2700 kg/m³, in the x-axis direction, the plate has a length of a = 0.6 m, and in the y-axis direction, the plate has a length of b = 0.6 m. The thickness of the plate (h) is 0.00625 m, 0.0125 m and, 0.025 m.

	h=0.00625 m			h=0.0125 m			h=0.025 m		
Mode Number	Exact sol. [23]	FEA [23]	Present study	Exact sol. [23]	FEA [23]	Present study	Exact sol. [23]	FEA [23]	Present study
1	136.5	135.8	135.8	273.1	271.7	269.8	546.2	543.5	530.6
2	262.5	259.9	260.91	525.2	519.8	517.2	1050.4	1039.7	1009.7
3	420.1	417.6	418.5	840.3	835.2	830.4	1680.7	1670.5	1618
4	472.7	466.8	469.9	945.4	933.7	930.3	1890.8	1867.5	1802.6
5	546.2	535.9	542.2	1092.5	1071.9	1071.1	2185.0	2143.7	2063.3
6	756.35	733.7	749.3	1512.7	1467.5	1474.9	3025.4	2935.1	2809.4
7	766.85	757.1	762.2	1533.7	1514.4	1504.8	3067.4	3028.7	2881
8	892.9	888.3	888.3	1785.8	1776.6	1753.3	3571.6	3553.3	3345.3
9	1018.9	997.8	1011	2037.9	2024.2	1987.9	4075.9	4048.3	3758.8
10	1050.4	1012.1	1039.8	2100.9	2263.4	2039.6	4201.9	4526.9	3838

Table 4: A comparison of natural frequencies (Hz) for simply supported rectangular plates of different thicknesses, based on the analytical solution and Ramu [23].

Tab. 4 presents a comparison of natural frequencies (Hz) for simply supported rectangular plates with different thicknesses, based on the analytical solution and Ramu [23]. The results closely match those obtained by Ramu [23] and the analytical solutions across various plate thicknesses.
As a second validation study, the free vibration behavior of a square sandwich plate with two-ply laminated face sheets arranged in a (0/90/C/90/0) stacking sequence is examined. Each laminate layer has a thickness of 0.05h, while the core accounts for 0.8h of the total thickness. The boundary condition type used is CCCC, indicating that all four edges are fully clamped. The analysis is conducted for aspect ratios of a/h=20, 10, and 5. The material properties of face sheets are defined as follows: E_{11f}=276 Gpa, $E_{22f}=G_{12f}=G_{13f}=G_{23f}$=6.9 Gpa, υ_{12f}=0.25 and ϱ_f=681.8 kg/m³. The material properties of core are defined as follows: $E_{11c}=E_{22c}$=0.5776 Gpa, $G_{12c}=G_{13c}$=0.1079 Gpa, G_{23c}=0.2221 Gpa, υ_{12c}=0.0025 and ϱ_c=1000 kg/m³. The dimensionless frequency parameters, defined as $\Omega=100(\omega a)(\varrho_c/E_{111f})$, corresponding to the first six vibration modes, are listed in Tab. 5 as obtained using the Ansys model. Tab. 5 clearly shows that the outcomes obtained using the present Ansys model closely match the numerical results reported in the literature.

a/h	References	Mode no. 1	2	3	4	5	6
20	Present	9.999	14.903	16.932	20.317	21.191	25.339
	Belarbi, Tati [24]	10.253	15.530	17.605	21.217	22.568	26.107
	Khandelwal, Chakrabarti [25]	10.330	15.598	17.644	21.246	22.354	26.636
	Chalak, Chakrabarti [26]	10.336	15.609	17.659	21.278	22.368	26.683
	Kulkarni and Kapuria [27]	10.332	15.600	17.674	21.404	22.323	26.893
	Chakrabarti and Sheikh [28]	10.536	14.709	18.708	20.182	21.369	25.406
10	Present	10.791	15.791	18.163	21.573	21.917	26.418
	Belarbi, Tati [24]	11.318	16.967	19.332	23.187	24.428	27.934
	Khandelwal, Chakrabarti [25]	11.349	16.900	19.214	23.003	23.925	28.502
	Chalak, Chakrabarti [26]	11.356	16.909	19.236	23.041	23.935	28.539
	Kulkarni and Kapuria [27]	11.468	17.135	19.494	23.659	24.253	28.918
	Chakrabarti and Sheikh [28]	11.524	15.691	19.946	20.783	22.356	25.812
5	Present	11.022	16.076	18.638	22.028	22.125	26.775
	Belarbi, Tati [24]	12.200	18.733	21.120	25.614	27.959	29.866
	Khandelwal, Chakrabarti [25]	12.121	18.453	20.706	25.058	26.849	30.908
	Chalak, Chakrabarti [26]	12.138	18.469	20.764	25.138	26.860	31.050
	Kulkarni and Kapuria [27]	12.440	19.106	21.442	26.691	28.043	32.257
	Chakrabarti and Sheikh [28]	11.864	15.672	19.477	20.057	21.167	23.628

Table 5: Non-dimensional frequency values (Ω) for a square sandwich plate featuring laminated face sheets in a (0/90/C/90/0) configuration under fully clamped (CCCC) boundary conditions.

As a third validation study, free vibration analysis of the beam made of 3D printed PETG material with clamped-free and clamped-clamped boundary conditions was performed. The material properties are defined as follows:
E=1660 Mpa, the density of the beam is ϱ=1270 kg/m^3, and the poison's ratio of the beam is υ=0.419. The length of the beam in the x-axis direction is a = 0.3 m, and the width in the y-axis direction is b = 0.03 m. The thickness of the beam (h) is 0.003 m. Tab. 6 presents a comparison of the natural frequencies (Hz) of a 3D printed PETG beam with different boundary conditions based on the experimental and finite element method results of Kannan, Ramamoorthy [20]. Tab. 6 demonstrates that the results derived from the current Ansys model are in strong agreement with both the numerical and experimental findings available in literature.

Mode Number	Clamped-free Experimental (Hz) [20]	ANSYS (Hz) [20]	Present study (Hz)	Clamped-clamped Experimental (Hz) [20]	ANYSY (Hz) [20]	Present study (Hz)
1	9.3	8.86	8.98	52	56.42	57.76
2	56	55.56	56.24	146	155.53	158.94
3	147.05	155.56	157.53	286	305.03	311.44
4	284.28	304.93.	309.09	485	504.84	514.92
5	484.21	504.61	511.76	728	756.04	769.34

Table 6: A comparison of the natural frequencies (Hz) of a 3D printed PETG beam with different boundary conditions based on the experimental and finite element method results of Kannan, Ramamoorthy [20].

Parametric study

Figs. 8, 9, 10, and 11 show the variation of the first four natural frequencies of 3D-printed PA6 plates with clamped boundary conditions on all four sides, for various configurations and aspect ratios of 1, 1.5, 2, and 2.5, respectively. Upon examining the graphs, it is observed that the highest natural frequencies are obtained in the H configuration, which has a stacking sequence of 100%-40%-100%. The lowest natural frequencies are found in the C configuration with a stacking sequence of 40%-100%-40%. When all three layers have the same infill ratio, the natural frequencies, from highest to lowest, are observed in the G, A, and D configurations, respectively. The stiffness and density values of PA6 material increase as the infill ratio increases from 40% to 100%. In the G configuration, which has a 100% infill ratio, the increase in structural stiffness is more dominant compared to the increase in density and moment of inertia, resulting in higher natural frequencies. Additionally, in configurations where the surface layers have the same infill ratio and the core layer has a different infill ratio, the natural frequencies of the structure decrease as the core layer's infill ratio increases. For instance, among the A, B, and

C configurations, the highest natural frequencies are observed in configuration A, while the lowest are in configuration C. This is because as the core layer's infill ratio increases, both the stiffness and the density of the structure increase. However, the increase in density has a more significant effect than the increase in stiffness, leading to a decrease in natural frequencies. Moreover, when the core material has the same infill ratio, the natural frequencies of the structures increase as the infill ratio of the surface materials increases. For example, among the A, E, and H configurations with a core infill ratio of 40%, the highest natural frequencies are observed in configuration H, while the lowest are in configuration A. This is due to the fact that as the infill ratio of the surface materials increases, the structural stiffness also increases. A stiffer surface layer enhances the flexural rigidity of the structure, thus increasing the natural frequencies. Furthermore, the graphs reveal that as the aspect ratio increases, the natural frequencies also increase due to the corresponding increase in structural stiffness.

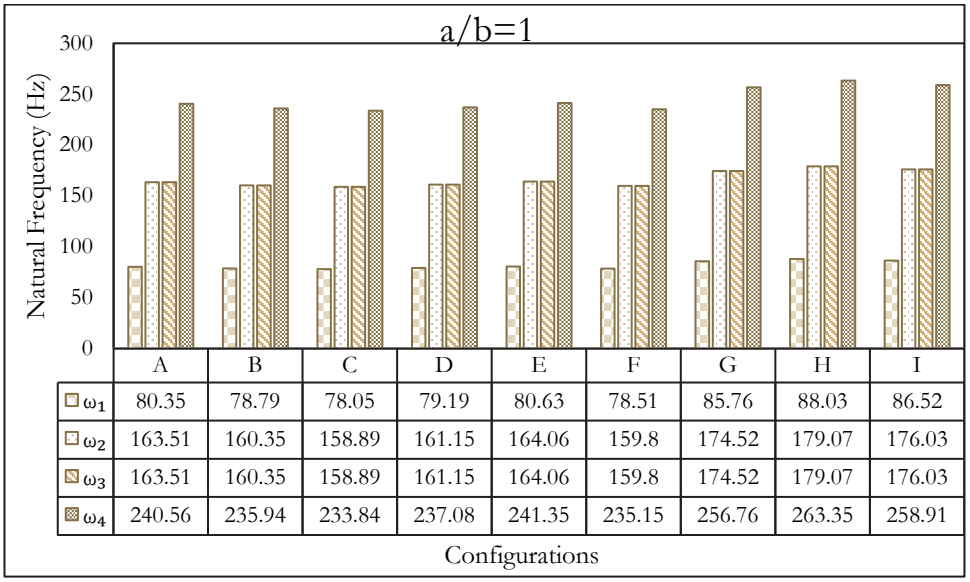

	A	B	C	D	E	F	G	H	I
ω_1	80.35	78.79	78.05	79.19	80.63	78.51	85.76	88.03	86.52
ω_2	163.51	160.35	158.89	161.15	164.06	159.8	174.52	179.07	176.03
ω_3	163.51	160.35	158.89	161.15	164.06	159.8	174.52	179.07	176.03
ω_4	240.56	235.94	233.84	237.08	241.35	235.15	256.76	263.35	258.91

Figure 8: Variation of the natural frequencies of 3D-printed PA6 plates with fully clamped boundary conditions and an aspect ratio of a/b =1 for various configurations.

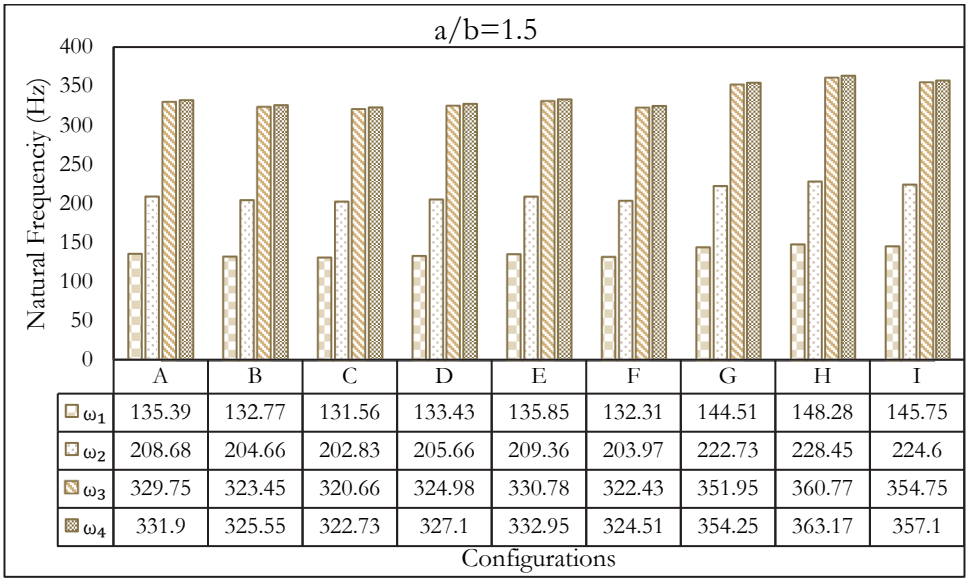

	A	B	C	D	E	F	G	H	I
ω_1	135.39	132.77	131.56	133.43	135.85	132.31	144.51	148.28	145.75
ω_2	208.68	204.66	202.83	205.66	209.36	203.97	222.73	228.45	224.6
ω_3	329.75	323.45	320.66	324.98	330.78	322.43	351.95	360.77	354.75
ω_4	331.9	325.55	322.73	327.1	332.95	324.51	354.25	363.17	357.1

Figure 9: Variation of the natural frequencies of 3D-printed PA6 plates with fully clamped boundary conditions and an aspect ratio of a/b =1.5 for various configurations.

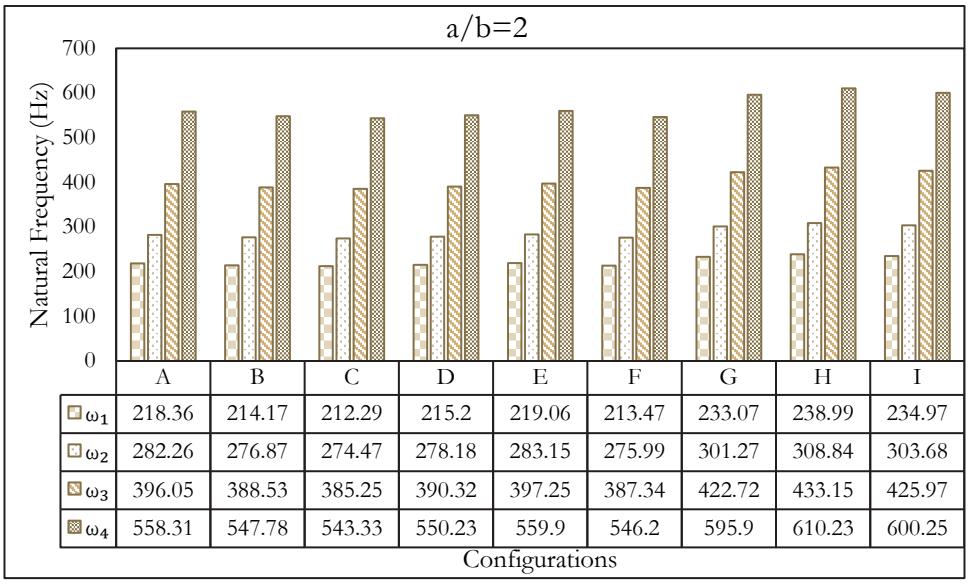

	A	B	C	D	E	F	G	H	I
ω_1	218.36	214.17	212.29	215.2	219.06	213.47	233.07	238.99	234.97
ω_2	282.26	276.87	274.47	278.18	283.15	275.99	301.27	308.84	303.68
ω_3	396.05	388.53	385.25	390.32	397.25	387.34	422.72	433.15	425.97
ω_4	558.31	547.78	543.33	550.23	559.9	546.2	595.9	610.23	600.25

Figure 10: Variation of the natural frequencies of 3D-printed PA6 plates with fully clamped boundary conditions and an aspect ratio of a/b =2 for various configurations.

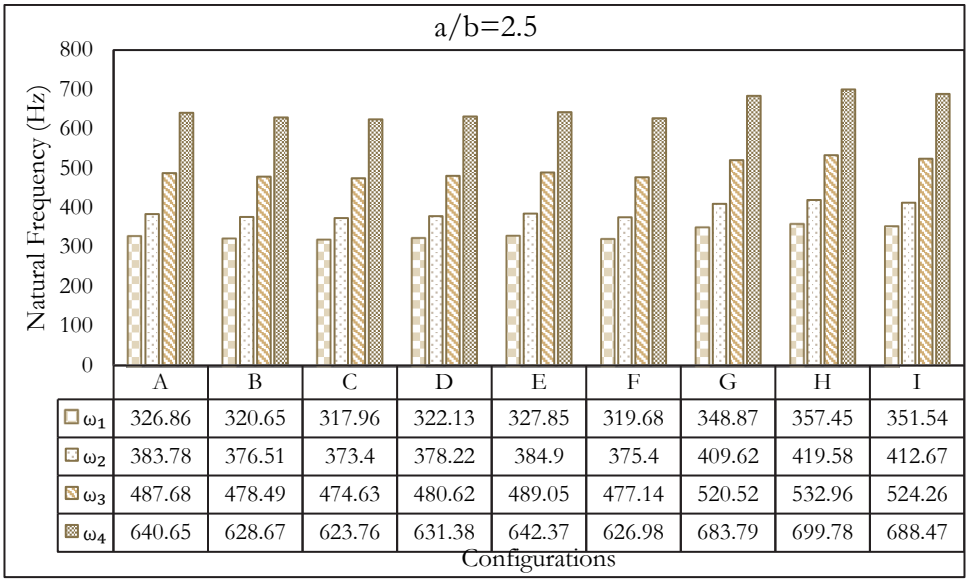

	A	B	C	D	E	F	G	H	I
ω_1	326.86	320.65	317.96	322.13	327.85	319.68	348.87	357.45	351.54
ω_2	383.78	376.51	373.4	378.22	384.9	375.4	409.62	419.58	412.67
ω_3	487.68	478.49	474.63	480.62	489.05	477.14	520.52	532.96	524.26
ω_4	640.65	628.67	623.76	631.38	642.37	626.98	683.79	699.78	688.47

Figure 11: Variation of the natural frequencies of 3D-printed PA6 plates with fully clamped boundary conditions and an aspect ratio of a/b =2.5 for various configurations.

Figs. 12, 13, 14, and 15 show the first, second, third, and fourth mode shapes, respectively, of the 3D-printed PA6 plate with H-configuration and CCCC boundary conditions for aspect ratios of a/b = 1, 1.5, 2.0, and 2.5, respectively.

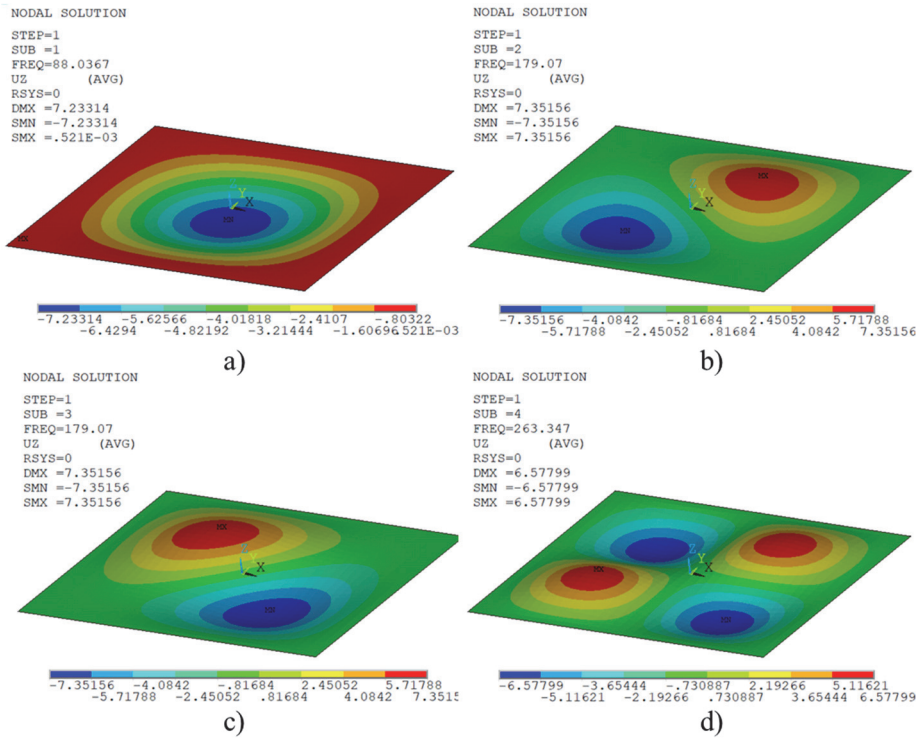

Figure 12: Mode shapes of the 3D-printed PA6 plate with H-configuration and CCCC boundary conditions for aspect ratio a/b =1: (a) Mode 1, (b) Mode 2, (c) Mode 3, (d) Mode 4.

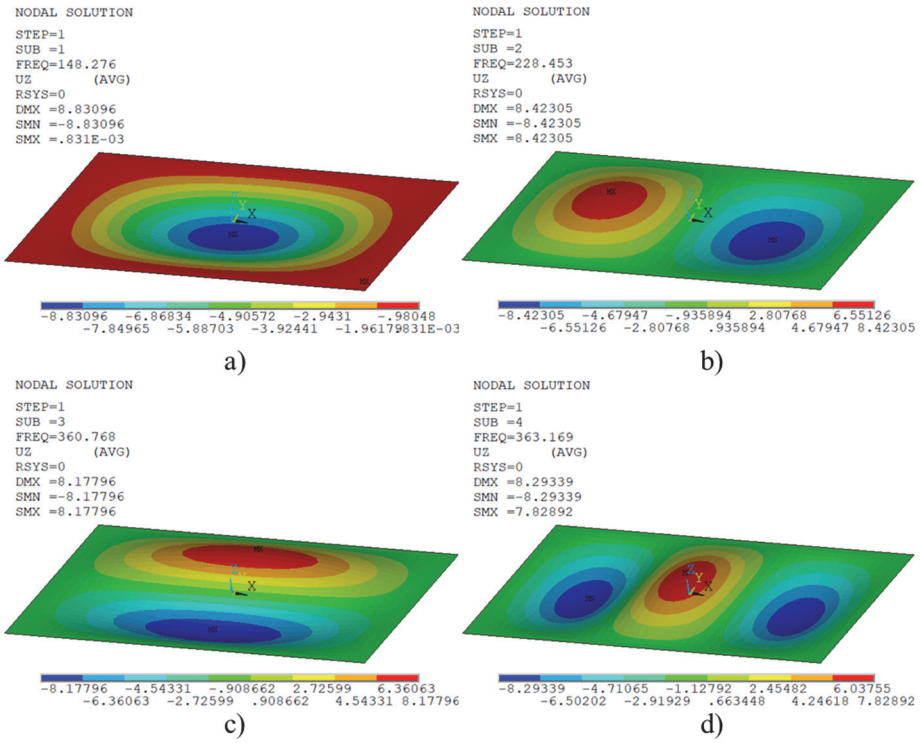

Figure 13: Mode shapes of the 3D-printed PA6 plate with H-configuration and CCCC boundary conditions for aspect ratio a/b =1.5: (a) Mode 1, (b) Mode 2, (c) Mode 3, (d) Mode 4.

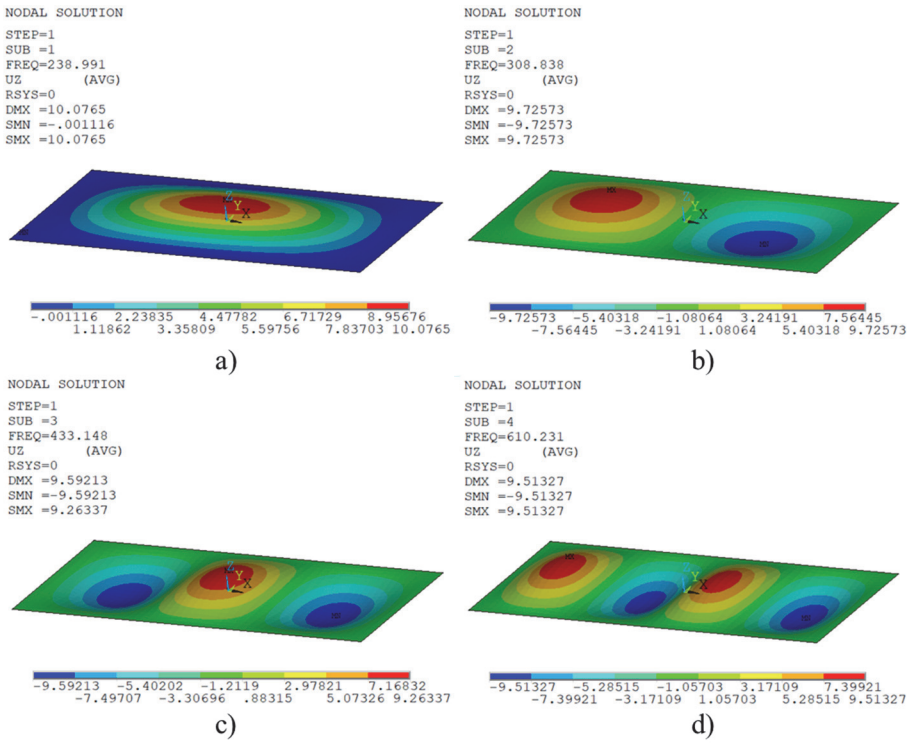

Figure 14: Mode shapes of the 3D-printed PA6 plate with H-configuration and CCCC boundary conditions for aspect ratio a/b =2: (a) Mode 1, (b) Mode 2, (c) Mode 3, (d) Mode 4.

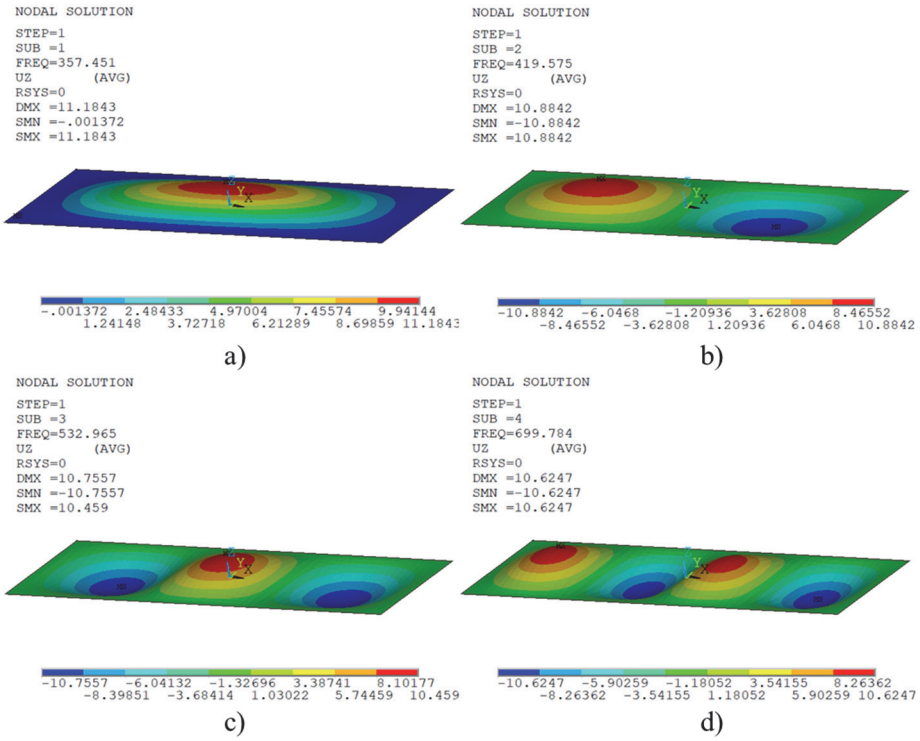

Figure 15: Mode shapes of the 3D-printed PA6 plate with H-configuration and CCCC boundary conditions for aspect ratio a/b =2.5: (a) Mode 1, (b) Mode 2, (c) Mode 3, (d) Mode 4.

Figs. 16, 17, 18, and 19 illustrate the variation in the first four natural frequencies of 3D-printed PA6 plates with simply supported edges on all sides (SSSS), corresponding to aspect ratios of 1.0, 1.5, 2.0, and 2.5, respectively, across various structural configurations. A detailed analysis of these figures indicates that the H configuration, characterized by a stacking sequence of 100%-40%-100% infill ratios, consistently yields the highest natural frequencies. In contrast, the C configuration, with its 40%-100%-40% sequence, demonstrates the lowest natural frequencies among the tested samples. When the infill ratio remains constant across all three layers, the order of natural frequencies from highest to lowest is observed in the G, A, and D configurations, respectively. This behavior can be attributed to the material properties of PA6, where both the stiffness and the density increase with a higher infill percentage. In the G configuration, which employs a uniform 100% infill ratio, the enhancement in structural stiffness has a more pronounced effect compared to the increase in mass and moment of inertia, thereby resulting in elevated natural frequencies. In configurations where the outer layers share the same infill percentage and the core layer varies, it is evident that an increase in the core infill ratio leads to a reduction in natural frequencies. For example, among configurations D, E, and F, the highest frequencies are found in E, and the lowest in F. Although increasing the core infill enhances both the stiffness and the mass of the structure, the increase in mass tends to outweigh the gain in stiffness, leading to a net decrease in the system's dynamic response. Similarly, for configurations with a constant core infill ratio (e.g., 70%), the natural frequencies increase as the infill ratio of the outer layers increases. This trend is evident when comparing configurations B, D, and I, where I exhibits the highest frequencies and B the lowest. The rise in outer layer stiffness significantly boosts the overall flexural rigidity of the plate, resulting in higher frequencies. Finally, the graphs also indicate a clear trend: as the aspect ratio increases, the natural frequencies tend to rise. This is primarily due to an associated increase in structural stiffness in the longitudinal direction, which enhances the plate's resistance to deformation under dynamic loading.

In addition to the effects of configuration and aspect ratio, the influence of boundary conditions on the dynamic response of the plates was also examined. Upon examining Figs. 8 through 11, which present the natural frequencies of 3D-printed PA6 plates with CCCC boundary conditions, and Figs. 20 through 23, which display those of plates with SSSS boundary conditions, it is observed that the plates with CCCC boundary conditions exhibit higher natural frequencies compared to those with SSSS boundary conditions. This is attributed to the fact that plates with CCCC boundary conditions possess greater structural stiffness than those with SSSS boundary conditions.

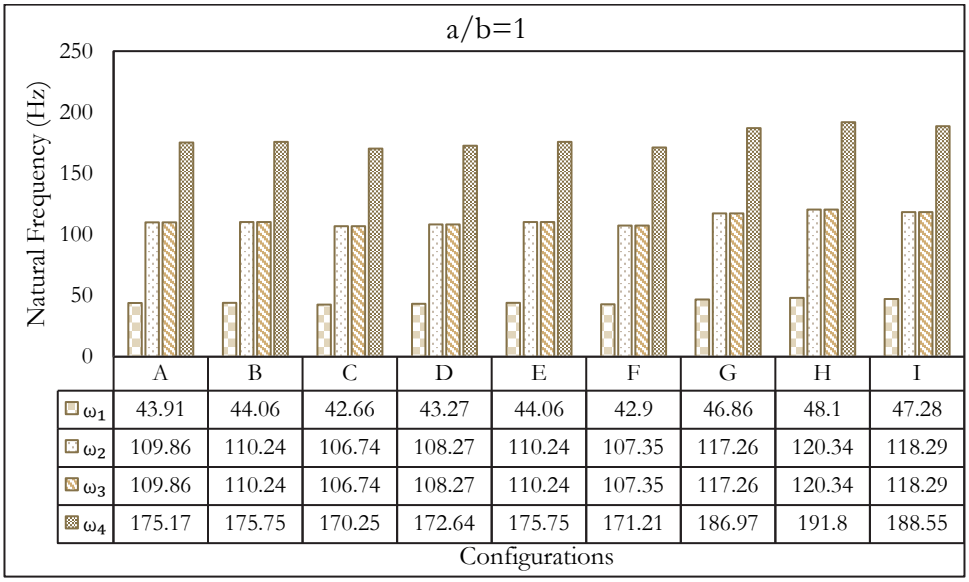

	A	B	C	D	E	F	G	H	I
ω_1	43.91	44.06	42.66	43.27	44.06	42.9	46.86	48.1	47.28
ω_2	109.86	110.24	106.74	108.27	110.24	107.35	117.26	120.34	118.29
ω_3	109.86	110.24	106.74	108.27	110.24	107.35	117.26	120.34	118.29
ω_4	175.17	175.75	170.25	172.64	175.75	171.21	186.97	191.8	188.55

Figure 16: Variation of the natural frequencies of 3D-printed PA6 plates with fully simple supported boundary conditions and an aspect ratio of a/b =1 for various configurations.

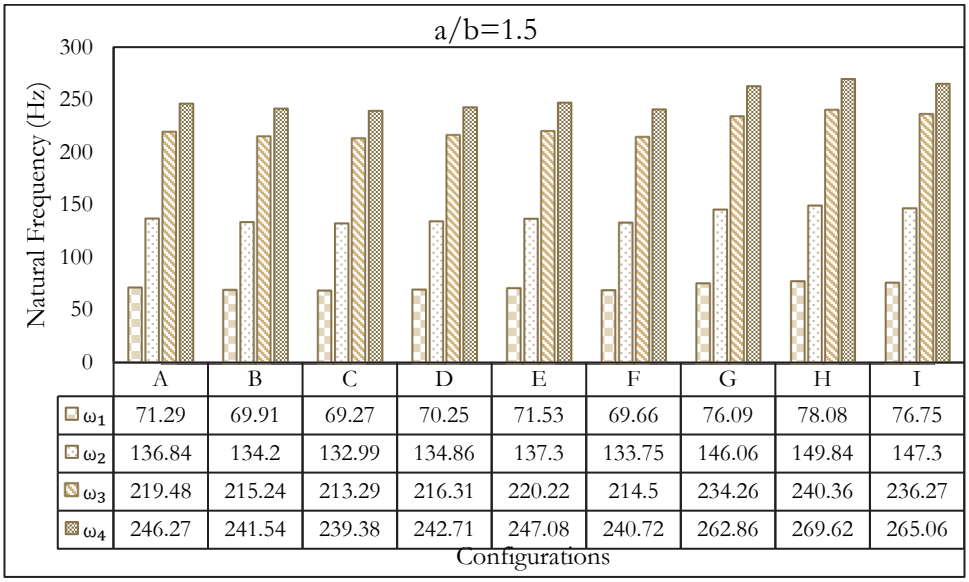

	A	B	C	D	E	F	G	H	I
ω_1	71.29	69.91	69.27	70.25	71.53	69.66	76.09	78.08	76.75
ω_2	136.84	134.2	132.99	134.86	137.3	133.75	146.06	149.84	147.3
ω_3	219.48	215.24	213.29	216.31	220.22	214.5	234.26	240.36	236.27
ω_4	246.27	241.54	239.38	242.71	247.08	240.72	262.86	269.62	265.06

Figure 17: Variation of the natural frequencies of 3D-printed PA6 plates with fully simple supported boundary conditions and an aspect ratio of a/b =1.5 for various configurations.

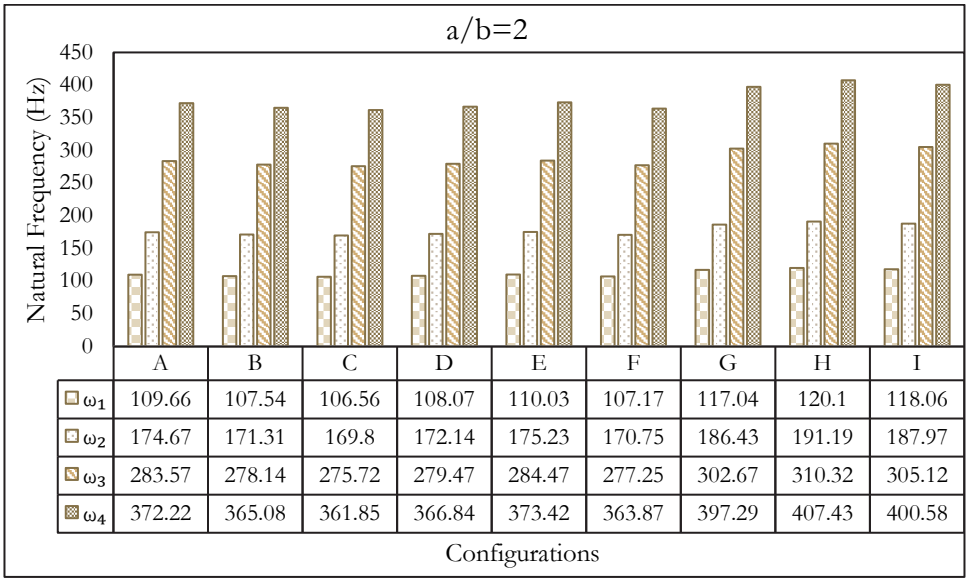

	A	B	C	D	E	F	G	H	I
ω_1	109.66	107.54	106.56	108.07	110.03	107.17	117.04	120.1	118.06
ω_2	174.67	171.31	169.8	172.14	175.23	170.75	186.43	191.19	187.97
ω_3	283.57	278.14	275.72	279.47	284.47	277.25	302.67	310.32	305.12
ω_4	372.22	365.08	361.85	366.84	373.42	363.87	397.29	407.43	400.58

Figure 18: Variation of the natural frequencies of 3D-printed PA6 plates with fully simple supported boundary conditions and an aspect ratio of a/b =2 for various configurations.

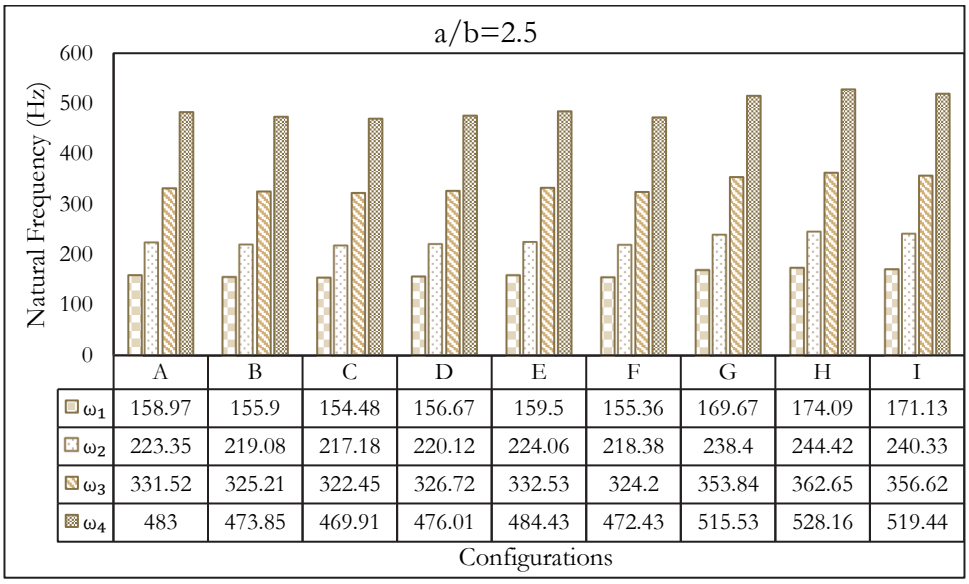

	A	B	C	D	E	F	G	H	I
ω_1	158.97	155.9	154.48	156.67	159.5	155.36	169.67	174.09	171.13
ω_2	223.35	219.08	217.18	220.12	224.06	218.38	238.4	244.42	240.33
ω_3	331.52	325.21	322.45	326.72	332.53	324.2	353.84	362.65	356.62
ω_4	483	473.85	469.91	476.01	484.43	472.43	515.53	528.16	519.44

Figure 19: Variation of the natural frequencies of 3D-printed PA6 plates with fully simple supported boundary conditions and an aspect ratio of a/b =2.5 for various configurations.

Figs. 20, 21, 22, and 23 present the first four mode shapes of the 3D-printed PA6 plate featuring an H-configuration and simply supported (SSSS) boundary conditions, corresponding to aspect ratios of a/b = 1.0, 1.5, 2.0, and 2.5, respectively.

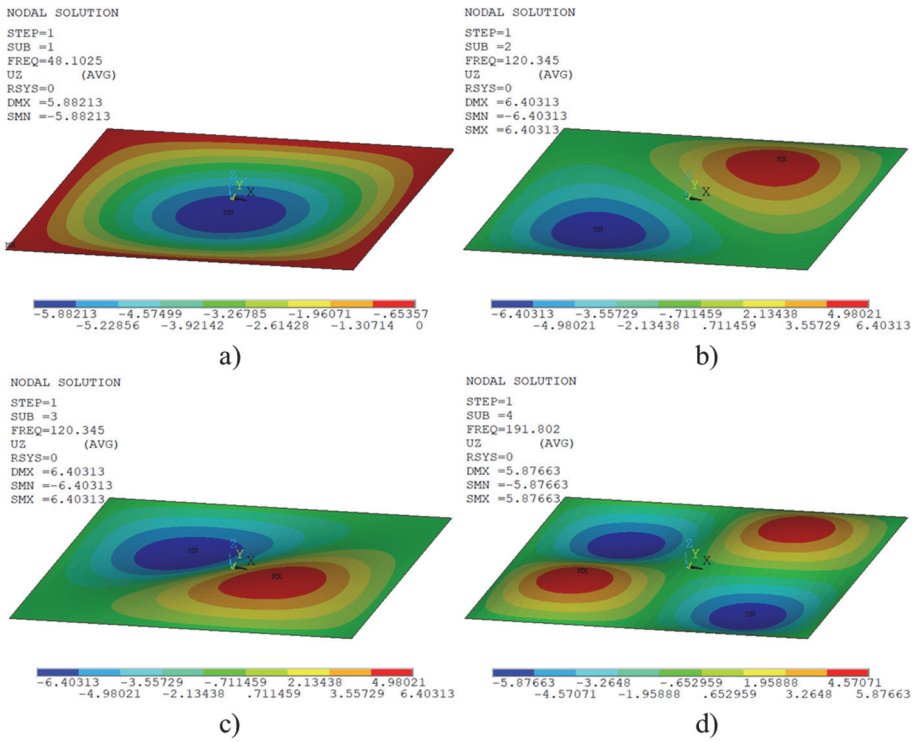

Figure 20: Mode shapes of the 3D-printed PA6 plate with H-configuration and SSSS boundary conditions for aspect ratio a/b =1: (a) Mode 1, (b) Mode 2, (c) Mode 3, (d) Mode 4.

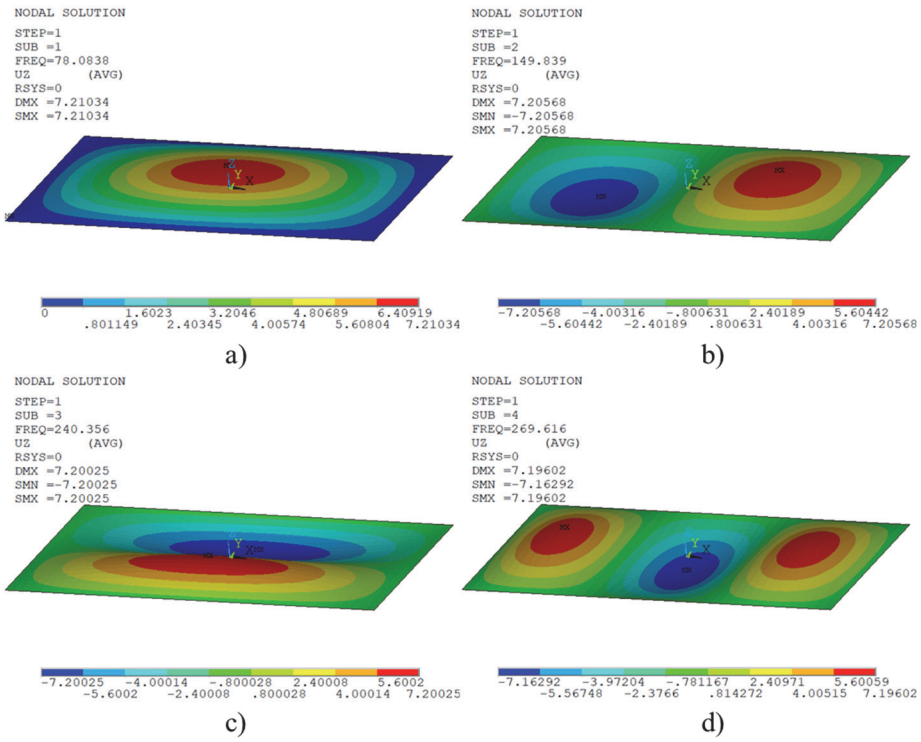

Figure 21: Mode shapes of the 3D-printed PA6 plate with H-configuration and SSSS boundary conditions for aspect ratio a/b =1.5: (a) Mode 1, (b) Mode 2, (c) Mode 3, (d) Mode 4.

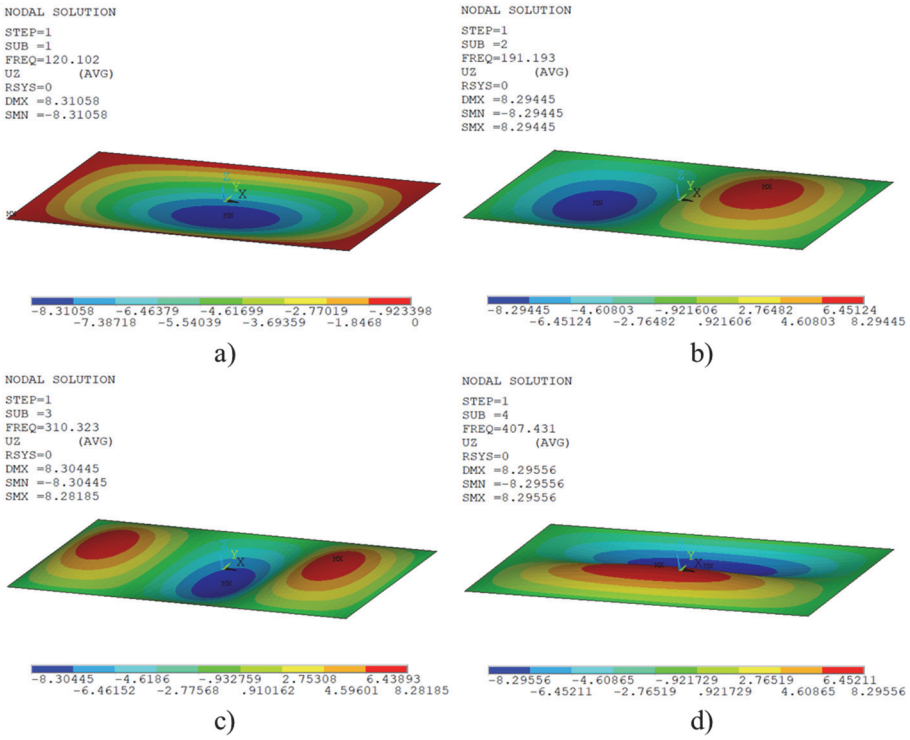

Figure 22: Mode shapes of the 3D-printed PA6 plate with H-configuration and SSSS boundary conditions for aspect ratio a/b =2: (a) Mode 1, (b) Mode 2, (c) Mode 3, (d) Mode 4.

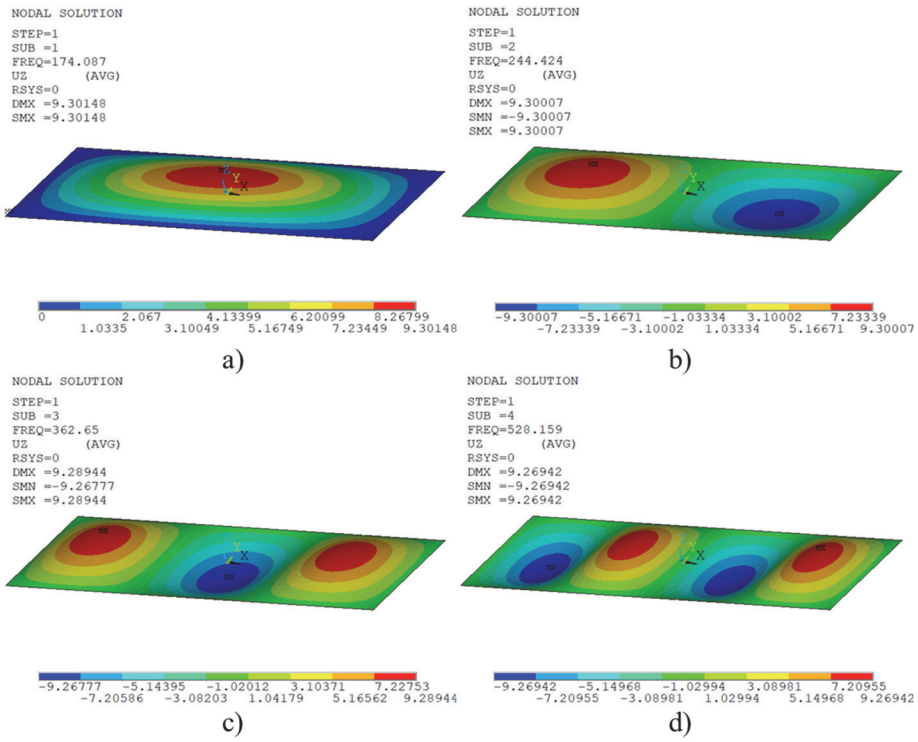

Figure 23: Mode shapes of the 3D-printed PA6 plate with H-configuration and SSSS boundary conditions for aspect ratio a/b =2.5: (a) Mode 1, (b) Mode 2, (c) Mode 3, (d) Mode 4.

Conclusion

In this study, the free vibration behavior of 3D-printed PA6 layered plates was comprehensively investigated by combining experimental tensile tests and finite element analyses. Unlike previous research, the combined influence of stacking sequence, infill ratio, aspect ratio, and boundary conditions was evaluated in detail for the first time in the literature. The findings reveal that the mechanical properties of PA6 samples, such as tensile strength, elastic modulus, and density, increase with higher infill ratios, primarily due to the reduction of internal voids and improved structural integrity. The vibration performance of the layered plates is significantly affected by the stacking sequence. Configurations with higher infill ratios in the surface layers and lower in the core (e.g., 100%-40%-100%) exhibited the highest natural frequencies, indicating that surface stiffness plays a dominant role in enhancing the flexural rigidity. Conversely, when the denser layer is placed in the core (e.g., 40%-100%-40%), natural frequencies decrease due to the dominant effect of mass increase over stiffness gain. This inverse relationship highlights the trade-off between stiffness and mass in determining dynamic performance. In configurations with equal core infill ratios, increasing the infill in surface layers leads to higher natural frequencies. This is attributed to the increased structural stiffness provided by stiffer outer layers, which contributes more effectively to resisting vibrational deformations. On the other hand, when the surface layers are kept constant and the core infill ratio is varied, natural frequencies tend to decrease as the core becomes denser, due to the relatively greater influence of mass addition compared to stiffness improvement. An increase in the plate aspect ratio leads to higher natural frequencies, as longer plates possess greater stiffness in the longitudinal direction, thus enhancing their resistance to dynamic excitation. Furthermore, boundary conditions have a notable influence on the vibrational response; plates with fully clamped edges exhibit significantly higher natural frequencies than those with simply supported edges, owing to the additional constraints and increased structural stiffness. The finite element model developed in ANSYS was validated using data from the literature and showed good agreement, confirming its reliability for predicting the dynamic behavior of 3D-printed PA6 structures. Overall, the study offers valuable insights into how infill distribution and geometric configurations can be optimized to improve the dynamic performance of polymer components. These results are particularly relevant for functional 3D-printed parts such as gears, fan blades, and robotic arms, where vibration control is essential for durability, operational stability, and energy efficiency.

REFERENCES

[1] Amroune, S., Belaadi, A., Zaoui, M., Menaseri, N., Mohamad, B., Saada, K., and Benyettou, R. (2021), Manufacturing of rapid prototypes of mechanical parts using reverse engineering and 3D Printing. J. Serbian Soc. Comput. Mech, 15(1), pp. 167-176.

[2] He, C., Ma, C., Li, X., Hou, F., Yan, L., Guo, A., and Liu, J. (2021), Continuous fast 3D printing of SiOC ceramic components. Additive Manufacturing, 46, pp. 102111.

[3] Ergene, B., Şekeroğlu, İ., Bolat, Ç., and Yalçın, B. (2021), An experimental investigation on mechanical performances of 3D printed lightweight ABS pipes with different cellular wall thickness. Journal of Mechanical Engineering and Sciences, 15(2), pp. 8169-8177.

[4] Thomas, A. and Mishra, U. (2022), A sustainable circular economic supply chain system with waste minimization using 3D printing and emissions reduction in plastic reforming industry. Journal of Cleaner Production, 345, pp. 131128.

[5] Bolat, Ç., Ergene, B., and Ispartalı, H. (2023), A comparative analysis of the effect of post production treatments and layer thickness on tensile and impact properties of additively manufactured polymers. International Polymer Processing, 38(2), pp. 244-256.

[6] Fico, D., Rizzo, D., Casciaro, R., and Esposito Corcione, C. (2022), A review of polymer-based materials for fused filament fabrication (FFF): focus on sustainability and recycled materials. Polymers, 14(3), pp. 465.

[7] Pazhamannil, R.V., Govindan, P., Edacherian, A., and Hadidi, H.M. (2024), Impact of process parameters and heat treatment on fused filament fabricated PLA and PLA-CF. International Journal on Interactive Design and Manufacturing (IJIDeM), 18(4), pp. 2199-2213.

[8] Bolat, Ç. and Ergene, B. (2024), Wear performance of short fiber added polyamide composites produced by additive manufacturing: Combined impacts of secondary heat treatment, reinforcement type, and test force. Polymer Composites, 45(8), pp. 6885-6900.

[9] Baraheni, M., Shabgard, M.R., and Tabatabaee, A.M. (2024), Effects of FDM 3D printing parameters on PLA biomaterial components dimensional accuracy and surface quality. Proceedings of the Institution of Mechanical Engineers, Part C: Journal of Mechanical Engineering Science, 238(9), pp. 3864-3873.

[10] Sharma, A., Chhabra, D., Sahdev, R., Kaushik, A., and Punia, U. (2022), Investigation of wear rate of FDM printed TPU, ASA and multi-material parts using heuristic GANN tool. Materials Today: Proceedings, 63, pp. 559-565.

[11] Vinoth Babu, N., Venkateshwaran, N., Rajini, N., Ismail, S.O., Mohammad, F., Al-Lohedan, H.A., and Suchart, S. (2022), Influence of slicing parameters on surface quality and mechanical properties of 3D-printed CF/PLA composites fabricated by FDM technique. Materials Technology, 37(9), pp. 1008-1025.

[12] Parpala, R.C., Popescu, D., and Pupaza, C. (2021), Infill parameters influence over the natural frequencies of ABS specimens obtained by extrusion-based 3D printing. Rapid Prototyping Journal, 27(6), pp. 1273-1285.

[13] Öteyaka, M.Ö., Çakir, F.H., and Sofuoğlu, M.A. (2022), Effect of infill pattern and ratio on the flexural and vibration damping characteristics of FDM printed PLA specimens. Materials Today Communications, 33, pp. 104912.

[14] Chaitanya, S.K., Reddy, K.M., and Harsha, S. (2015), Vibration properties of 3D printed/rapid prototype parts. Int. J. Innov. Res. Sci. Eng. Technol, 4(6), pp. 4602-4608.

[15] Bolat, Ç., Çebi, A., Maraş, S., and Ergene, B. (2024), An experimental and numerical effort on the vibration behavior of additively manufactured recycled polyethylene terephthalate glycol components. Polymer Engineering & Science, 64(11), pp. 5815-5830.

[16] Monkova, K., Monka, P.P., Vanca, J., Hricova, R., Knapcikova, L., Kozak, D., and Beno, P. (2021). Natural frequencies of a simple 3D printed lattice structure. 12th International Conference on Mechanical and Aerospace Engineering (ICMAE), IEEE, Athens, Greece, 16-19 July.

[17] Azmi, M., Ismail, R., Hasan, R., and Alkahari, M. (2018), Vibration Analysis of Fused Deposition Modelling Printed Lattice Structure Bar for Application in Automated Device. Int. J. Eng. Technol, 7, pp. 21-24.

[18] Kannan, S., Manapaya, A., and Selvaraj, R. (2023), Frequency and deflection responses of 3D-printed carbon fiber reinforced polylactic acid composites: Theoretical and experimental verification. Polymer Composites, 44(7), pp. 4095-4108.

[19] Ergene, B., Atlıhan, G., and Pinar, A.M. (2023), Experimental and finite element analyses on the vibration behavior of 3D-printed PET-G tapered beams with fused filament fabrication. Multidiscipline Modeling in Materials and Structures, 19(4), pp. 634-651.

[20] Kannan, S., Ramamoorthy, M., Sudhagar, E., and Gunji, B. Mechanical characterization and vibrational analysis of 3D printed PETG and PETG reinforced with short carbon fiber. in AIP Conference Proceedings. 2020. AIP Publishing.

[21] Zou, R., Xia, Y., Liu, S., Hu, P., Hou, W., Hu, Q., and Shan, C. (2016), Isotropic and anisotropic elasticity and yielding of 3D printed material. Composites Part B: Engineering, 99, pp. 506-513.
[22] Dudescu, C. and Racz, L. (2017), Effects of raster orientation, infill rate and infill pattern on the mechanical properties of 3D printed materials. ACTA Univ. Cibiniensis, 69(1), pp. 23-30.
[23] Ramu, I. and Mohanty, S. (2012), Study on free vibration analysis of rectangular plate structures using finite element method. Procedia engineering, 38, pp. 2758-2766.
[24] Belarbi, M.-O., Tati, A., Ounis, H., and Khechai, A. (2017), On the free vibration analysis of laminated composite and sandwich plates: a layerwise finite element formulation. Latin American journal of solids and structures, 14(12), pp. 2265-2290.
[25] Khandelwal, R.P., Chakrabarti, A., and Bhargava, P. (2013), Vibration and buckling analysis of laminated sandwich plate having soft core. International Journal of Structural Stability and Dynamics, 13(08), pp. 1350034.
[26] Chalak, H., Chakrabarti, A., Iqbal, M.A., and Sheikh, A.H. (2013), Free vibration analysis of laminated soft core sandwich plates. Journal of Vibration and Acoustics, 135(1), pp. 011013.
[27] Kulkarni, S. and Kapuria, S. (2008), Free vibration analysis of composite and sandwich plates using an improved discrete Kirchhoff quadrilateral element based on third-order zigzag theory. Computational mechanics, 42, pp. 803-824.
[28] Chakrabarti, A. and Sheikh, A. (2004), Vibration of laminate-faced sandwich plate by a new refined element. Journal of Aerospace Engineering, 17(3), pp. 123-134.